ISCI, Volume *9*

Supplemental Information

Biomechanics of Endothelial Tubule Formation Differentially Modulated by Cerebral Cavernous Malformation Proteins

Olga Chernaya, Anastasia Zhurikhina, Siarhei Hladyshau, William Pilcher, Katherine M. Young, Jillian Ortner, Vaishnavi Andra, Todd A. Sulchek, and Denis Tsygankov

SUPPLEMENTAL INFORMATION

Supplemental Figures

Figure S1. Related to Figure 1;

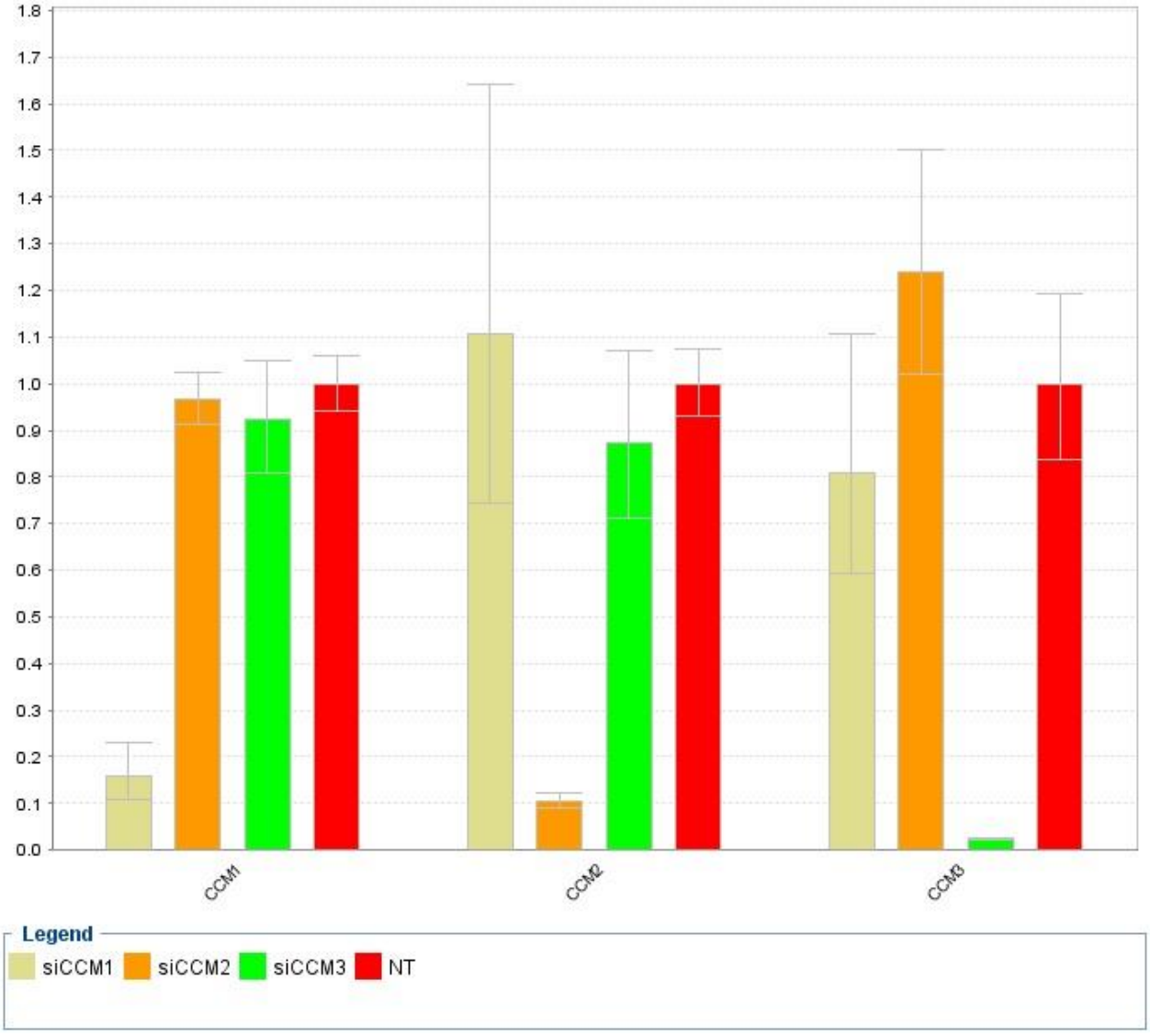

Figure S2. Related to Figure 2;

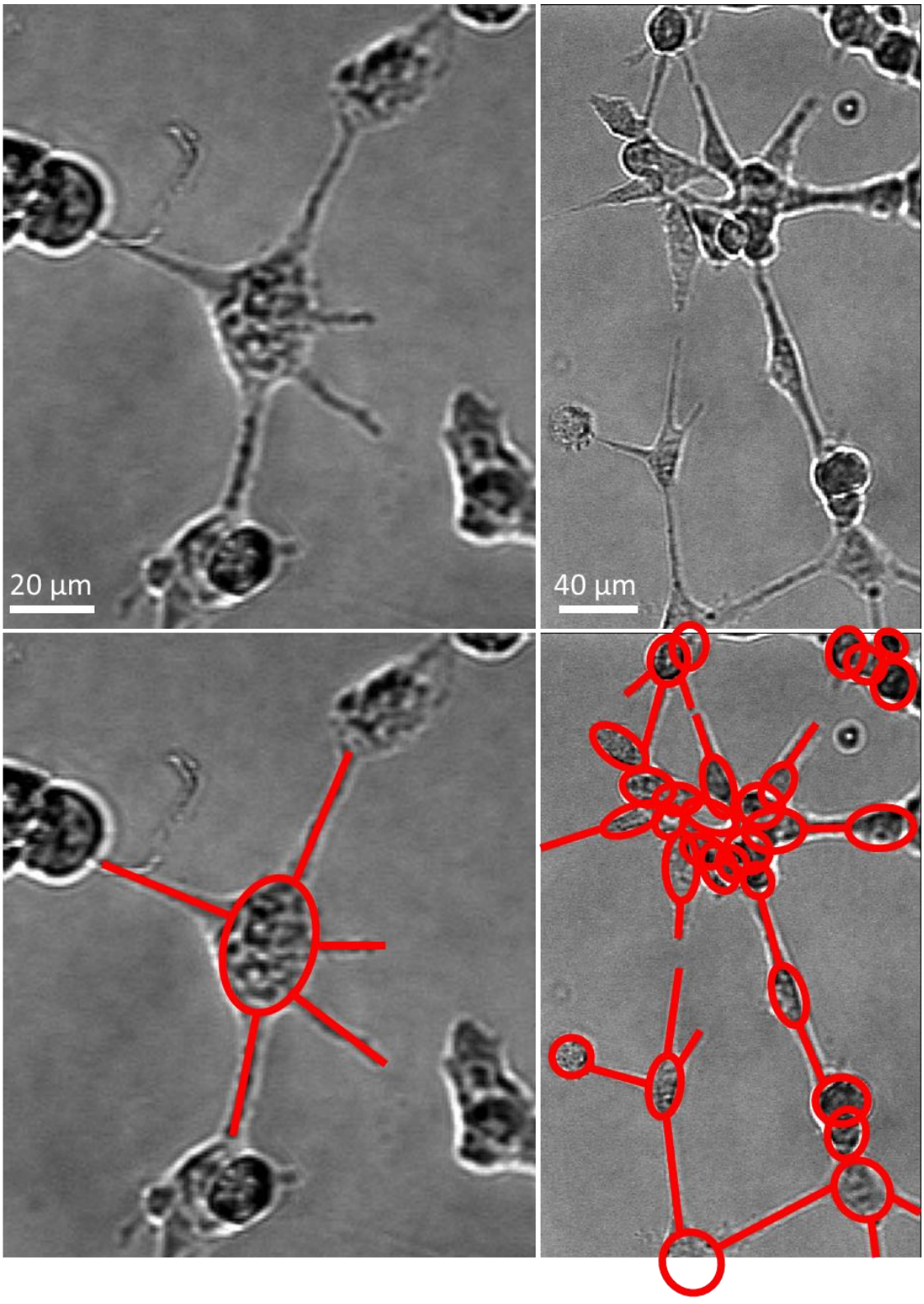

Figure S3. Related to Figure 2;

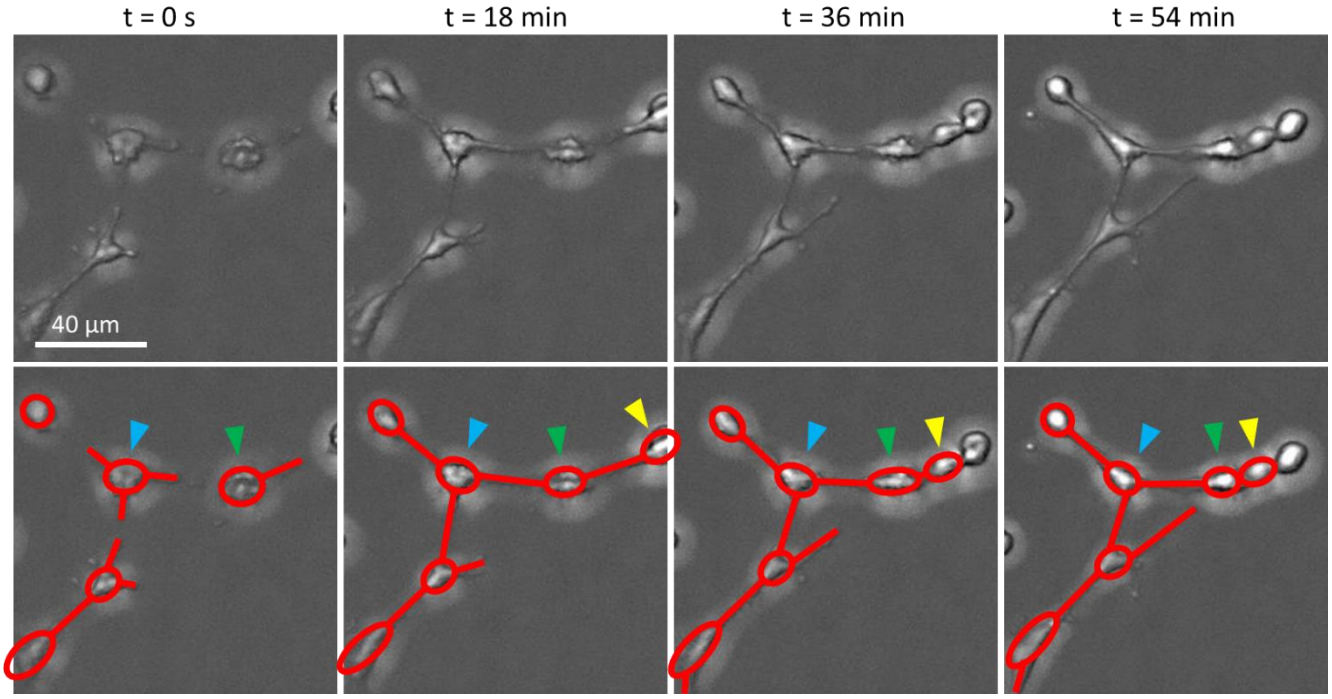

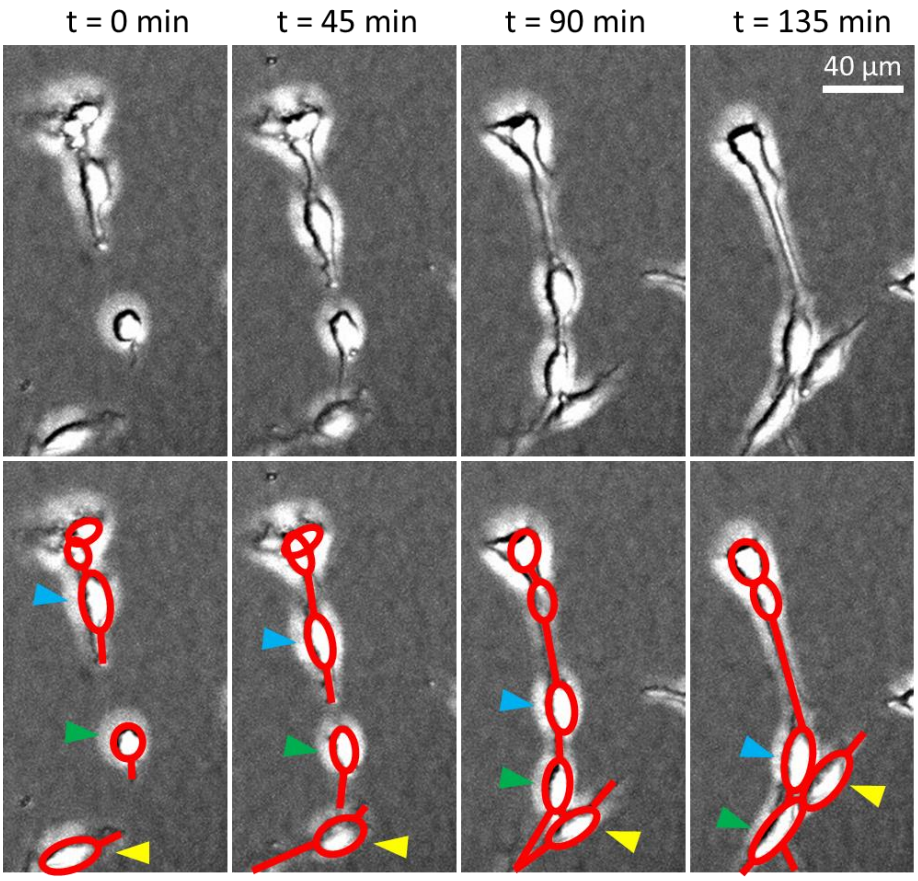

Figure S4. Related to Figure 2;

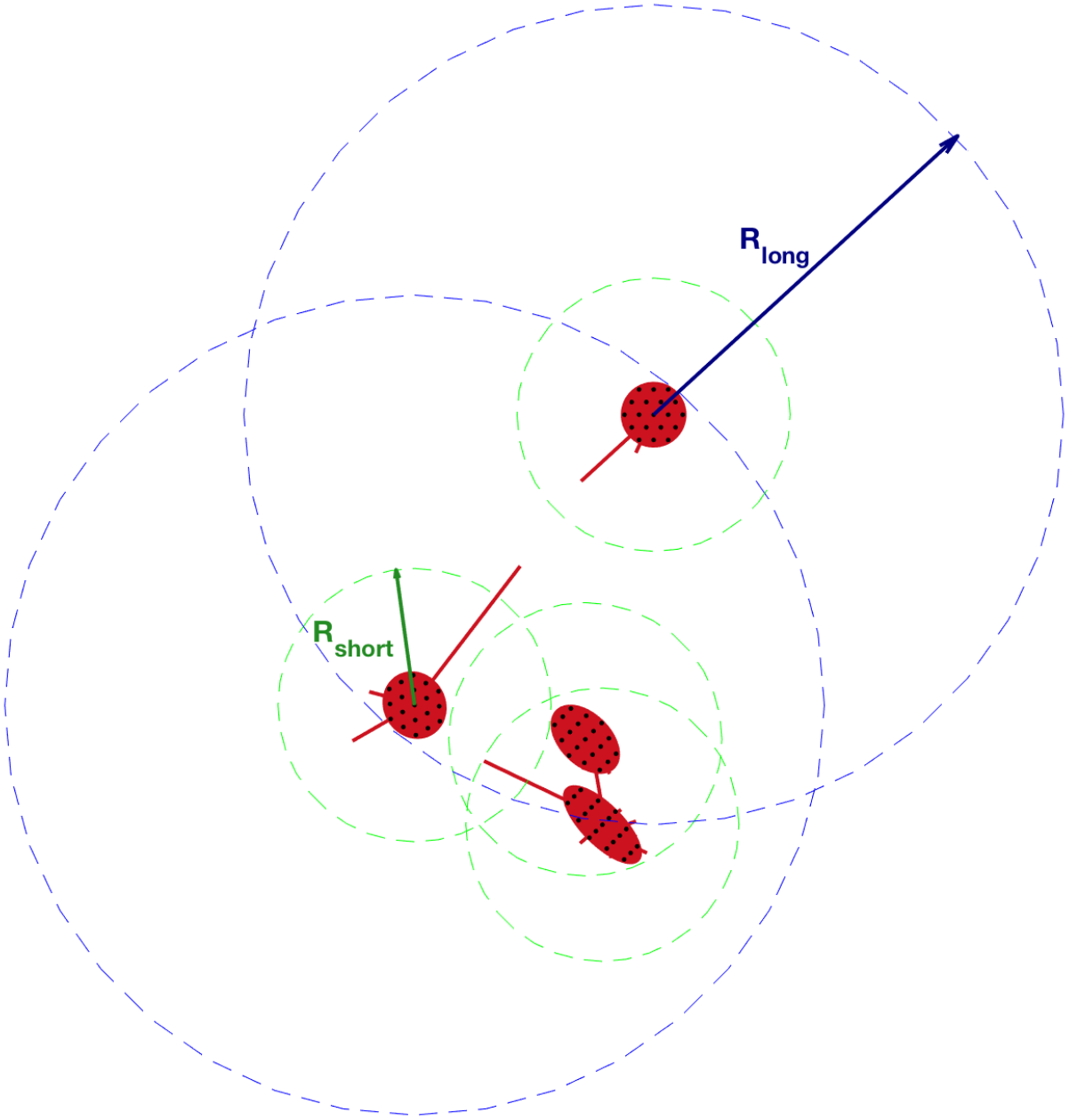

Figure S5. Related to Figure 2;

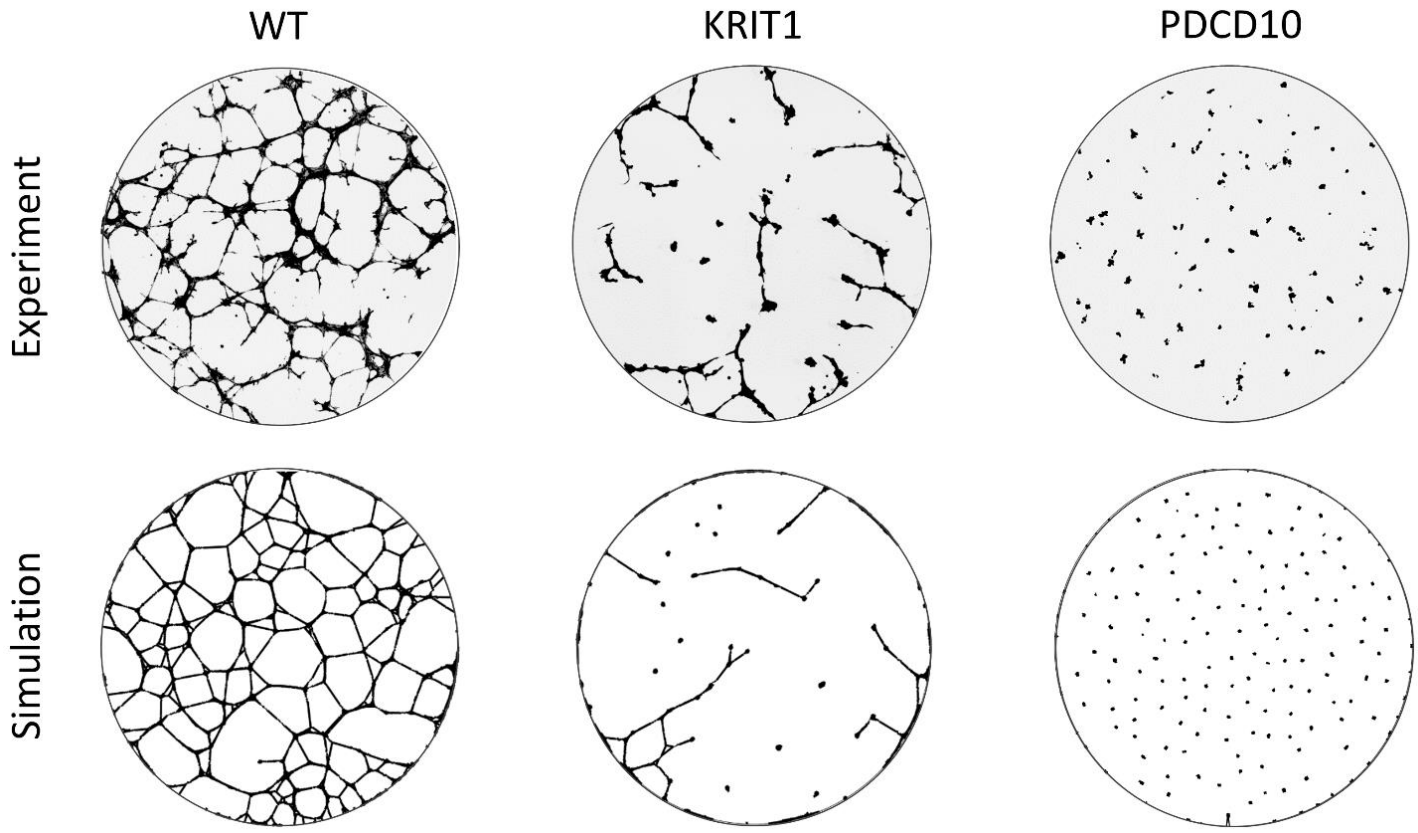

Figure S6. Related to Figure 2;

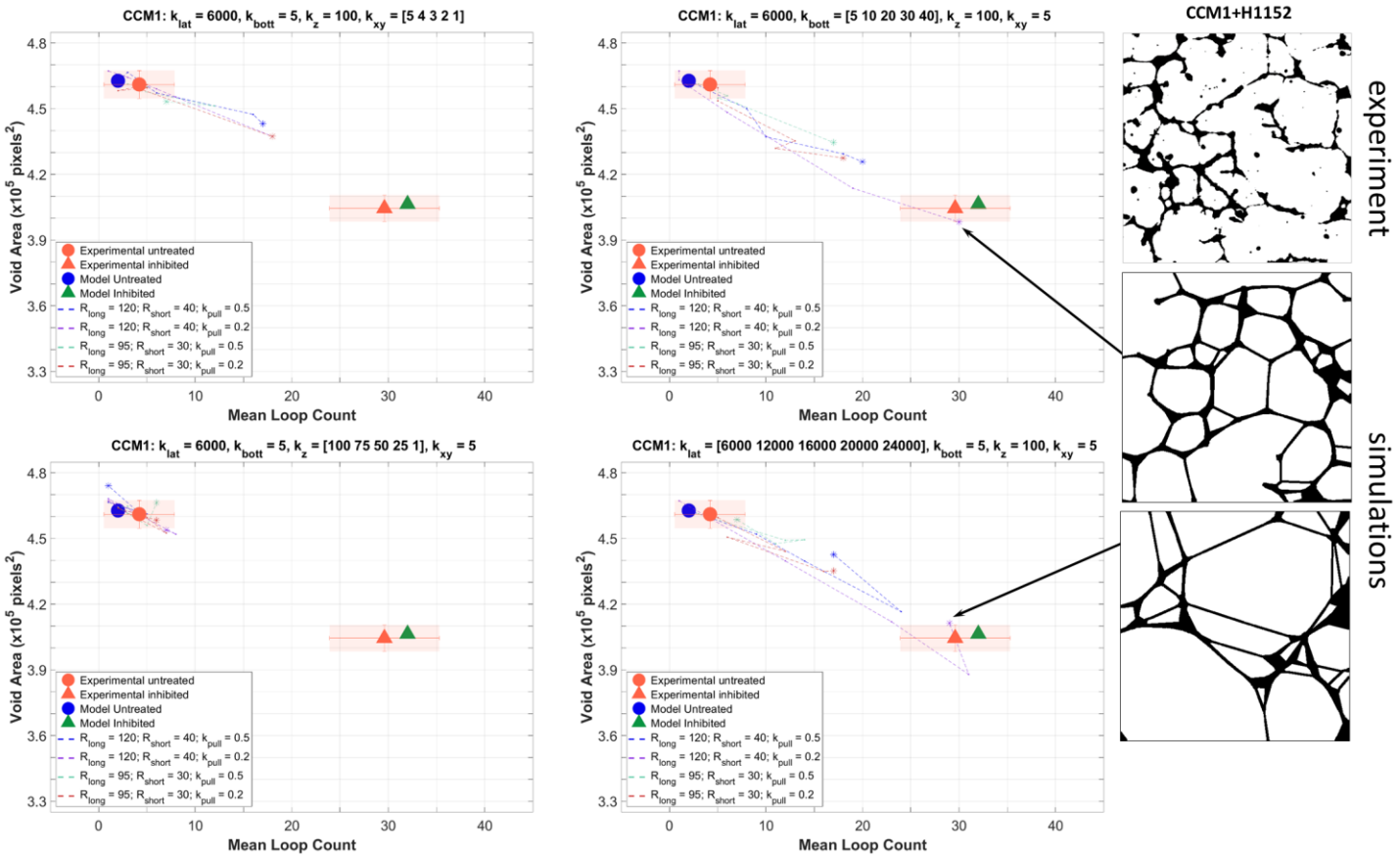

Figure S7

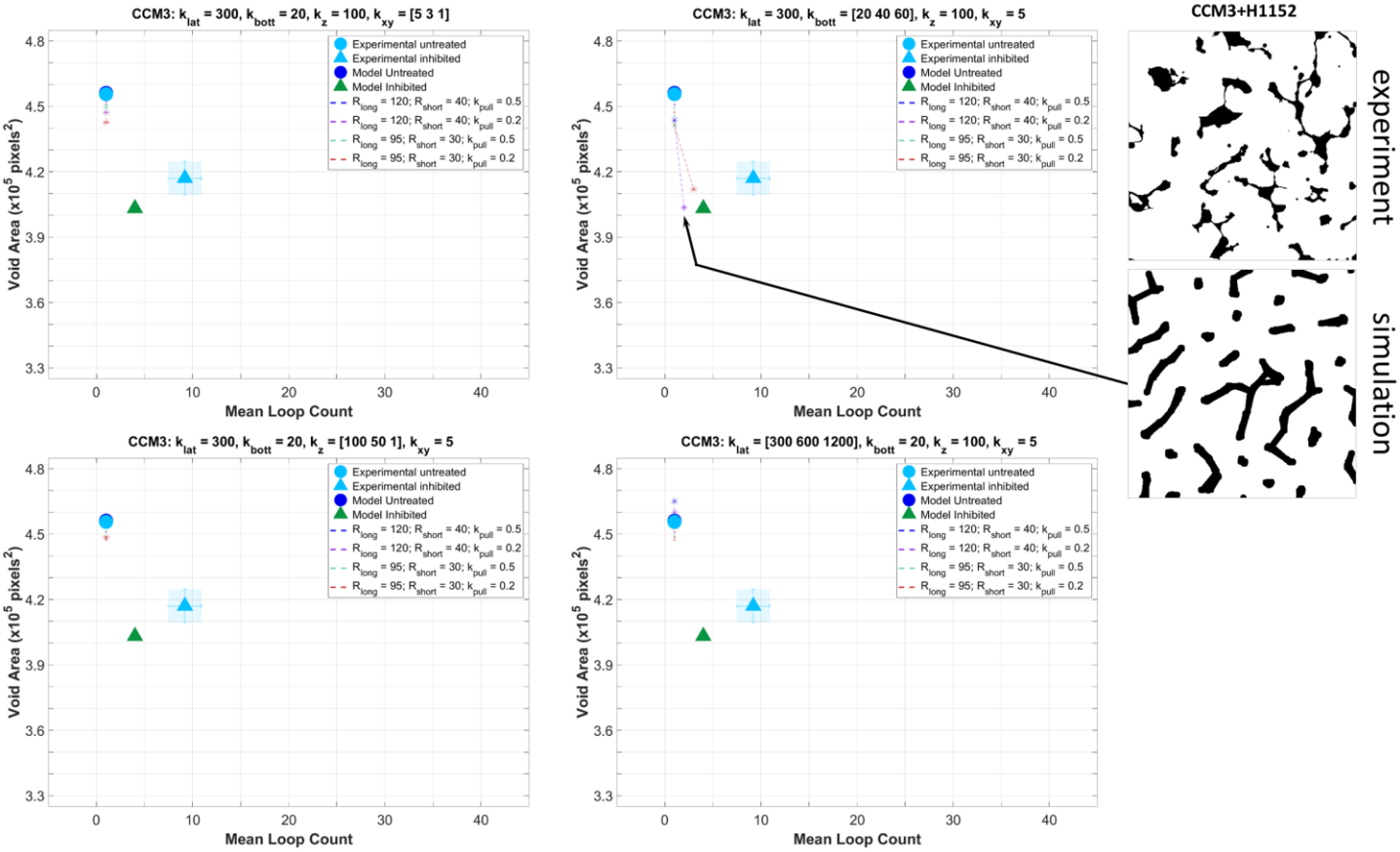

Figure S8. Related to Figure 2;

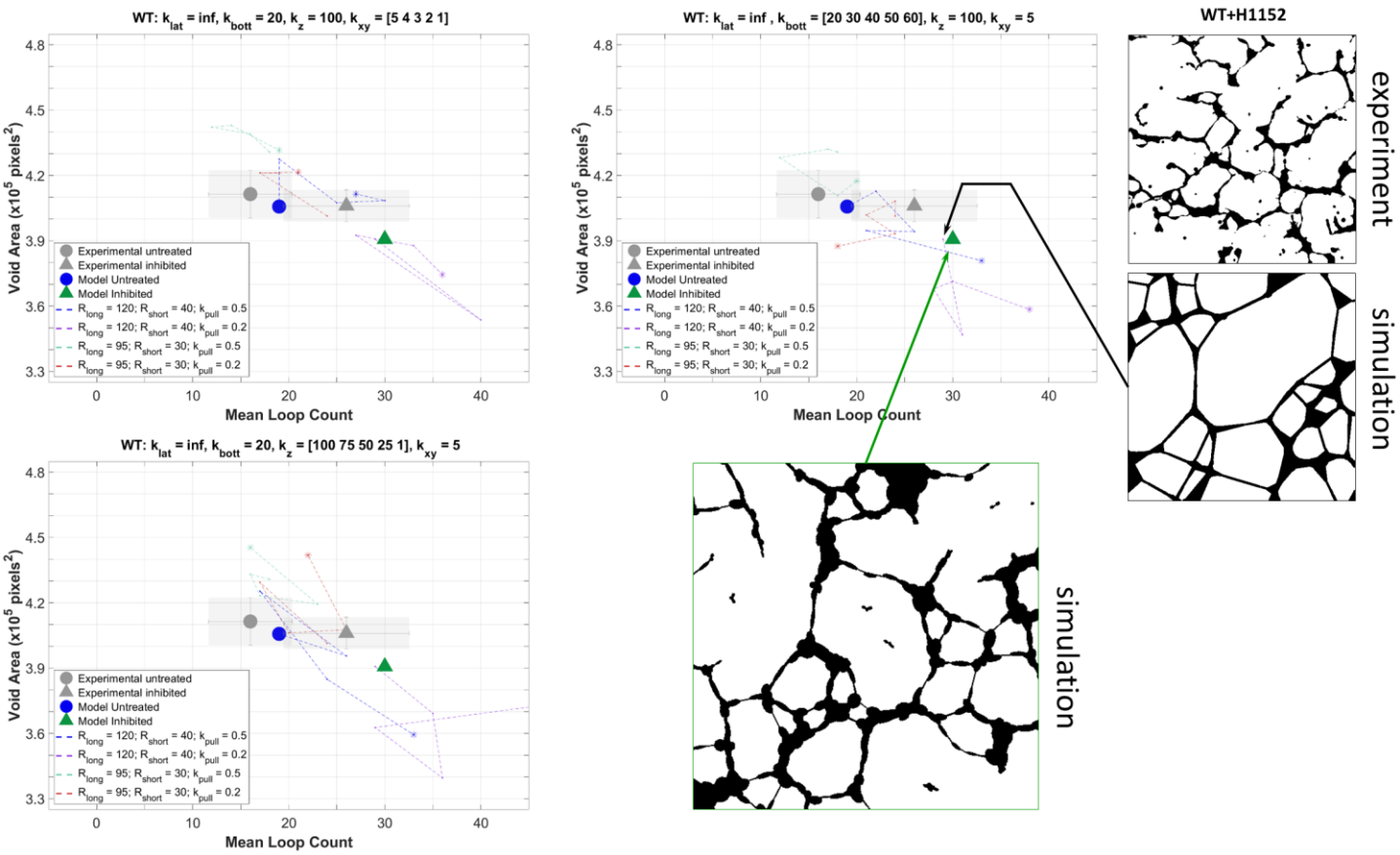

Figure S9. Related to Figure 4;

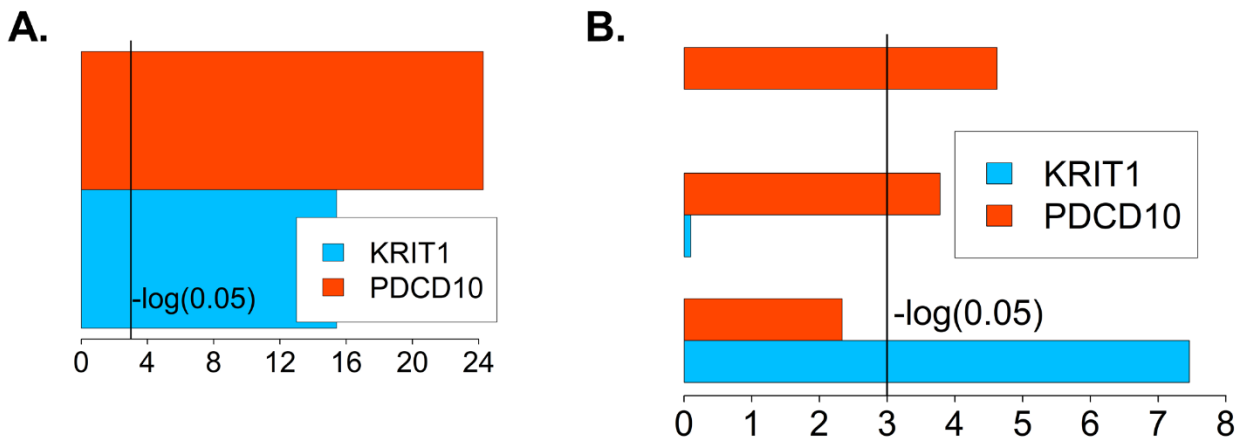

Figure S10. Related to Figure 4;

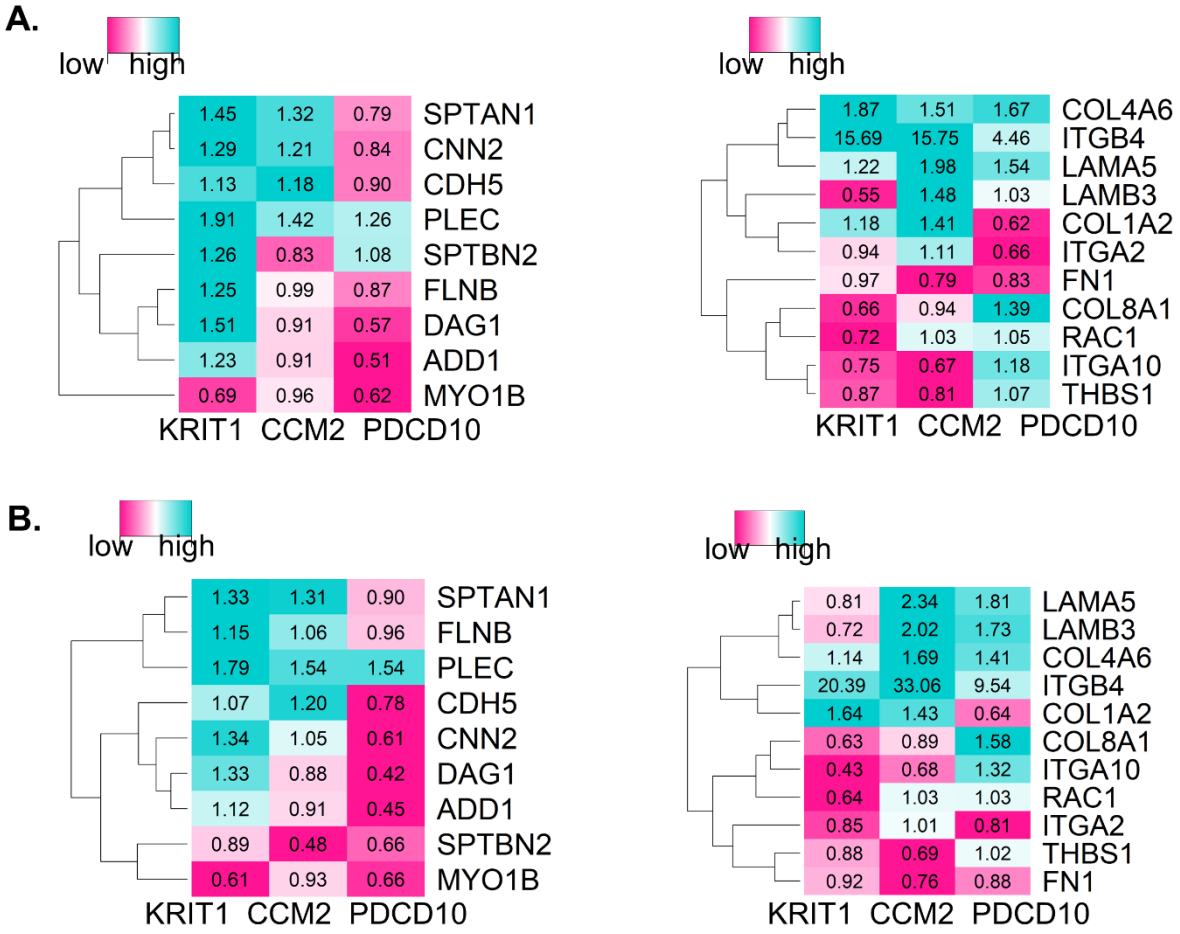

Supplemental Figure Legends

Figure S1: Bar graph demonstrating the efficiency of krit1, ccm2, and pdcd 10 mRNA expression knockdown at 48 hrs after siRNA transfection. Cells were treated as described under Material and Methods. Expression of each gene was analyzed by qPCR, normalized to expression of TBP, and compared to expression in cultures treated with non-target siRNA. The bars represent fold change in mRNA expression (Mean ± SD). Knockdown of expression of any of *ccm* genes did not have an effect on expression levels of the other 2 genes.

Figure S2: Two illustrative examples of cell shapes during the WT endothelial tube formation. In the bottom row, the experimental images from the top row are overplayed with the shapes formed by ellipses (representing cell bodies) and lines (either radially directed 'extending' protrusions or cell-cell attached 'pulling' protrusions). The reasonable accuracy of such simplified shape representation motivated the specifications of cell model in our simulations.

Figure S3: Two illustrative examples of cell shape dynamics during the WT endothelial tube formation. Similar to Figure S2, in the bottom rows in each time series, the experimental images from the top rows are overplayed with the shapes formed by deformable ellipses (representing cell bodies) and lines (either radially directed 'extending' protrusions or cell-cell attached 'pulling' protrusions). Colored arrowheads point to the same cells in each time frame to highlight the extent of cell displacement over the course of time. This dynamics of multicellular interactions through extending and retracting protrusions, which drives the movement and the deformation of cell bodies, motivated the specifications of the cell model in our simulations.

Figure S4: A schematic diagram illustrating the top view (xy-plane) of the cells soon after being platted on Matrigel. Blue and green circles demonstrate the long and short ranges of cell-cell sensing that guides the extension of the corresponding protrusions in the simulation model. Black dots distributed within elliptical cell bodies indicate the vertically directed (z −direction) protrusions, which are responsible for the cell-ECM interaction.

Figure S5: Experimental and simulated patterns of cells initially plated/distributed at equivalent densities (here 1600 cells in the field of view).
Top row: Experimental images of WT, KRIT1, and PDCP10 cell cultures.
Bottom row: Patterns resulted in the simulations of normal and disrupted cell-cell and cell-ECM interactions (same as Figure 2B, but with more cells in the simulations).

Figure S6: Parameter scans for the identification of regimes when void area and mean loop count measures of simulated patterns match the experimental values for KRIT1 KD cells. Experimental values for cultures treated and untreated with ROCK inhibitor (H1152) are shown by orange triangle and circle, respectively. The corresponding values from the simulations reported in the main text of the paper are shown by the green triangle and blue circle. The dash lines in the four graphs show the results from changing one of the parameters ($\kappa_{xy}, \kappa_{lat}, \kappa_z,$ and κ_{bott}) at a time. These results are compared for two regimes of cell-cell sensing (R_{long}, R_{short}) and two regimes of the pulling strength (κ_{pull}). The patterns on the right demonstrate that even when the void area and the mean loop count match experimental values, there are clear differences with regard to other geometric features. However, the trends identified with this scan suggests the combination of parameters that leads to a very close correspondence between the simulated and observed cell patterns (see also Figure 2C)

Figure S7: Parameter scans for the identification of regimes when void area and mean loop count measures of simulated patterns match the experimental values for PDCP10 KD cells. Experimental values for cultures treated and untreated with ROCK inhibitor (H1152) are shown by light blue triangle and circle, respectively. The corresponding values from the simulations reported in the main text of the paper are shown by the green triangle and blue circle. The dash lines in the four graphs show the results from changing one of the parameters ($\kappa_{xy}, \kappa_{lat}, \kappa_z,$ and κ_{bott}) at a time. These results are compared for two regimes of cell-cell sensing (R_{long}, R_{short}) and two regimes of the pulling strength (κ_{pull}). The patterns on the right demonstrate that even when the void area and the mean loop count approach experimental values, there are clear differences with regard to other geometric features. However, the trends identified with this scan suggests the combination of

parameters that leads to a very close correspondence between the simulated and observed cell patterns (see also Figure 2C)

Figure S8: Parameter scans for the identification of regimes when void area and mean loop count measures of simulated patterns match the experimental values for WT cells. Experimental values for cultures treated and untreated with ROCK inhibitor (H1152) are shown by gray triangle and circle, respectively. The corresponding values from the simulations reported in the main text of the paper are shown by the green triangle and blue circle. The dash lines in the four graphs show the results from changing one of the parameters ($\kappa_{xy}, \kappa_z,$ and κ_{bott}) at a time. These results are compared for two regimes of cell-cell sensing (R_{long}, R_{short}) and two regimes of the pulling strength (κ_{pull}). The patterns on the right demonstrate that even when the void area and the mean loop count approach experimental values, there are clear differences with regard to other geometric features. However, the trends identified with this scan suggests the combination of parameters that leads to a very close correspondence between the simulated and observed cell patterns (see also Figure 2C)

Figure S9: Enrichment analysis of differentially expressed genes.
A). Genes associated with cell-cell adhesion in 2D cultures. The graph shows negative log(p-values) for KRIT1 KD cells (blue bars) and PDCD10 cells (red bars) compared to WT cells.
B). Term enrichment for KRIT1 and PDCD10 KD endothelial cells at 2 hours after plating on Matrigel.

Figure S10: Differentially expressed genes involved in cell-cell and cell-ECM adhesion.
A). Heat map of a subset of differentially expressed genes involved in cell-cell (*left*) and cell-ECM (*right*) adhesion in cells cultured under 2D conditions. Text annotation represents fold change of RPKM values in comparison to WT cells.
B). Heat map of a subset of differentially expressed genes involved in cell-cell (*left*) and cell-ECM (*right*) adhesion in cells cultured on Matrigel for 2 hrs.

Supplemental Tables

Table S1. Related to Figure 1B;

P-Values (Void Area)	WT	WT-H1152	CCM1	CCM1-H1152	CCM2	CCM2-H1152	CCM3	CCM3-H1152
WT		0.446672191	0.000227504	0.311436311	0.022358986	0.004723167	0.001329989	0.427082125
WT-H1152	0.446672191		8.92353E-06	0.749524401	0.00334343	0.007518726	0.000180833	0.075260431
CCM1	0.000227504	8.92353E-06		3.91874E-06	0.003510728	7.07116E-05	0.171501257	4.68367E-05
CCM1-H1152	0.311436311	0.749524401	3.91874E-06		0.002820809	0.011538089	8.11118E-05	0.036487194
CCM2	0.022358986	0.00334343	0.003510728	0.002820809		0.000223636	0.012074674	0.038153775
CCM2-H1152	0.004723167	0.007518726	7.07116E-05	0.011538089	0.000223636		0.000233538	0.001642225
CCM3	0.001329989	0.000180833	0.171501257	8.11118E-05	0.012074674	0.000233538		0.000579579
CCM3-H1152	0.427082125	0.075260431	4.68367E-05	0.036487194	0.038153775	0.001642225	0.000579579	

P-Values (Mean Loop Count)	WT	WT-H1152	CCM1	CCM1-H1152	CCM2	CCM2-H1152	CCM3	CCM3-H1152
WT		0.043594134	0.004233614	0.006651511	0.207586693	0.008019723	0.002289809	0.033187737
WT-H1152	0.043594134		0.001133036	0.433314131	0.010062099	0.769664482	0.001574521	0.007667694
CCM1	0.004233614	0.001133036		0.000285754	0.021079927	8.14552E-05	0.154842121	0.056159092
CCM1-H1152	0.006651511	0.433314131	0.000285754		0.002106554	0.522263806	0.000546202	0.002342745
CCM2	0.207586693	0.010062099	0.021079927	0.002106554		0.001129274	0.004401545	0.236695303
CCM2-H1152	0.008019723	0.769664482	8.14552E-05	0.522263806	0.001129274		0.000262217	0.0005683
CCM3	0.002289809	0.001574521	0.154842121	0.000546202	0.004401545	0.000262217		0.000676315
CCM3-H1152	0.033187737	0.007667694	0.056159092	0.002342745	0.236695303	0.0005683	0.000676315	

Table S2. Related to Figure 2;

Main model Parameters/Constants			
Parameter Name	**Parameter description**	**Value**	**Units**
κ_{lat}	A constant defining the probability of cell-ECM contacts breakage: $P_{\text{cell-cell}} = 1 - \exp(-l^2/k_{lat}^2)$	∞ (WT); 6000 (CCM1); 300 (CCM3)	μm
κ_{bott}	A constant defining the probability of cell-ECM contacts breakage: $P_{\text{cell-ECM}} = 1 - \exp(-l^2/k_{bott}^2)$	20 (WT); 5 (CCM1); 20 (CCM3)	μm
κ_z	Spring constant representing cytoskeletal resistance to vertical deformations (spreading)	100 · S	N/m
κ_{xy}	Spring constant representing cytoskeletal resistance to in-plane deformations (stretching)	5 · S	N/m
κ_{pull}	Spring constant of cell-cell and cell-ECM contact	0.5 · S	N/m
R_{long}	The maximal extent of long-range protrusions (the range of cell-cell sensing)	120	μm
R_{short}	The maximal extent of short-range protrusions	40	μm
R_{bott}	The attachment range of ventral protrusions	2.6	μm
N_{bott}	The maximal number of bottom protrusions	19	1
N_{long}	The maximal number of long-range protrusions	5	1
N_{lim}	The limit on the number of extending protrusions	15	1
$u_{prot}\ (lateral)$	Growth rate of lateral protrusions in the 'extending' mode	0.017	μm /s
$u_{prot}\ (bottom)$	Growth rate of ventral protrusions in the 'extending' mode	0.003	μm /s
u_{retr}	Retraction rate of lateral protrusions in the 'pulling' mode	0.003	μm /s
η_{xy}	Viscous drag in response to *x* and *y* displacement	0.4 · S	N*s/m
η_{ab}	Viscous drag in response to cell body elongation	20 · S	N*s/m
η_{φ}	Viscous drag in response to cell rotation (in *xy*-plane)	0.13 · S	N*s/m
η_{ξ}	Viscous drag in response to the shift of protrusions bases with respect to the semi-principle axes (in *xy*-plane)	0.6 · S	N*s/m
R_0	Mean radius of individual cells	6.32	μm
R_{box}	Dish radius (simulation domain)	863 (Figs. 2); 1600 (S.Fig. 3)	μm
N	Total number of cells	466 (Figs. 2); 1600 (S.Fig. 3)	1
D	Density of cells per plating area	0.0002 $(N/\pi R_{box}^2)$	1/μm^2
S	Arbitrary scaling parameter	-	unitless

Table S3. Related to Figure 4;

WT /2D	KRIT1 /2D	CCM2 /2D	PDCD10 /2D
WT /3D-2hrs	KRIT1 /3D-2hrs	CCM2 /3D-2hrs	PDCD10 /3D-2hrs
WT /3D-6hrs	KRIT1 /3D-6hrs	CCM2 /3D-6hrs	PDCD10 /3D-6hrs

Supplemental Table Legends

Table S1: Comparison of Void area and Mean loop count in untreated and treated with ROCK inhibitor WT and KD cells.
Green: $p \leq 0.05$ for pair-wise comparison in Student's t-test
Red: $p > 0.05$ for pair-wise comparison in Student's t-test.

Table S2. Model parameters.
Green: parameters defining cell-cell and cell-matrix interactions
Yellow: parameters defining protrusion and retraction rates
Orange: force-velocity coefficients for the system's coordinates
Blue: parameters defining cell size, number, and the simulation domain.

Table S3: Genotypes and cell cultures conditions analyzed by RNA-sequencing.

Transparent Methods

Cell culture

Human umbilical cord endothelial cells HUVEC (Lonza, Walkersville, MD) were maintained in EGM-2 medium (Lonza) at 37°C/5% CO_2 and passaged every 3 to 4 days for up to 6 passages at a 1:5 sub-culturing ratio. For tube formation experiments, 4.5-5x10^3 cells were plated into each well of angiogenesis µ-slides (ibidi, Fitchburg, WI) coated with 10 µl of growth factor reduced phenol red-free Matrigel (Corning, Corning, NY), and incubated for up to 18 hrs.

Microscopy

Cells plated on Matrigel-coated glass coverslips were fixed in 4% para-formaldehyde for 10 min, permeabilized with 0.1% Triton X100/PBS for 5 min. Actin filaments were stained with rhodamine-phalloidin (Molecular Probes, Carlsbad, CA), and nuclei were counterstained with DAPI (Molecular Probes, Carlsbad, CA). The cells were imaged using a Zeiss LSM 700 confocal microscope.
For time-lapse imaging of endothelial tubule formation, cells plated on Matrigel were incubated with CellMask™ Green Plasma Membrane Stain (Invitrogen, Carlsbad, CA) for 15 min at 37°C, the media was changed to phenol-free EGM-2 supplemented with 2% FBS and growth factors (PromoCell GmbH). Images were acquired using PerkinElmer UltraVIEW VoX spinning disk confocal microscope (PerkinElmer, Waltham, MA). Image processing and analysis were performed using ImageJ software (NIH).

Gene expression knockdown

To achieve knockdown of CCM protein expression, cells were infected with PLKO.1 vector based lentiviruses carrying shRNAs for human *krit1* (RHS4533-EG889), *ccm2* (RMM4534-EG216527), and *pdcd10* (RHS4533-EG11235) genes (Dharmacon, Lafayette, CO). Lentiviral particles, prepared and purified by VectorBuilder technical service group (VectorBuilder, Santa Clara, CA) were added to EGM-2 media supplemented with 8µ/mL polybrene for 48 hrs. Transduced cells were selected through their resistance to puromycin added to the growth media in the concentration of 2.5 µg/ml. Expression knockdown was measured by real-time PCR with TaqMan gene expression assays. Phenotypic experiments were conducted between 6 and 10 days after infection.
Where indicated, cells were transfected with 50 nM siRNA against human *krit1* (LQ-003825-00), *ccm2* (LG-014728-01), and *pdcd10* (LQ-004436-00), or control non-targeting siRNA (D-001810-01-05), using DharmaFECT 4 transfection reagent (all from Dharmacon, Lafayette, CO). Gene expression was analyzed at 48 hrs, protein expression at 72 hrs after transfection, and phenotypic studies were conducted 60-72 hrs after transfection.

Real-time PCR

Total RNA was extracted using RNeasy extraction kit (Qiagen, Valencia, CA, USA) following the manufacturer's protocol. RNA was reverse-transcribed using the high-capacity cDNA kit (Life Technologies, Carlsbad, CA, USA). The analysis was done StepOnePlus™ Real-Time PCR System (Applied Biosystems, Foster City, CA), and the level of transcripts was quantified using TaqMan probes (Applied Biosystems): KRIT1 Hs01090981_m1; CCM2 Hs01123856_m1; PDCD10 Hs00200578_m1; TBP Hs00427620_m1. Fold change in gene expression was determined using $\Delta\Delta C_t$ algorithm.

Adhesion assay

Adhesion assays were performed in 96-well plates coated with growth factor-reduced Matrigel. 1x10^4 cells were plated in each well, and allowed to attach for 30 min at 37°C. To remove non-adherent cells, growth media was replaced and the adherent cells were incubated for additional 2 hrs in fresh media containing 20 µl of 5 mg/mL of Thiazolyl Blue Tetrazolium Bromide, MTT (Sigma-Aldrich, St. Louis, MO). Following incubation, the cells were lysed in 10% Triton X100 in acidic isopropanol, and an absorbance at 590 nm was determined.

Western Blotting

Cells were lysed in RIPA buffer supplemented with protease inhibitor cocktail, sonicated briefly, and cleared by centrifugation and boiled in Laemmli SDS sample buffer. 10 µg of protein per lane was separated by SDS-PAGE and transferred to nitrocellulose membranes. Membranes were blocked and incubated overnight at +4°C with primary antibodies against KRIT1, CCM2, PDCD10, phosphorylated myosin light chain (ThermoFisher Scientific, Rockford, IL) phosphorylated cofilin, and actin (Novus Biologicals, Littleton, CO). Next, membranes were incubated with HRP-conjugated secondary antibodies (all from ThermoFisher Scientific, Rockford, IL), and developed using West Pico PLUS chemiluminescent substrate (ThermoFisher Scientific, Rockford, IL).

RNA sequencing

HUVEC cells were transfected with non-targeting siRNA or siRNA against *krit1*, *ccm2*, and *pdcd10* genes as described above. 48 hrs after transfection cells were plated on growth factor reduced Matrigel, and incubated for 2 hrs (initial stages of endothelial tubule formation) or 6 hrs (advanced stages of tubule formation). Total RNA was isolated from each culture (control, and siRNA against *krit1*, *ccm2*, and *pdcd10*) cells cultured on the 2D (Matrigel-coated plastic), and in 3D (Matrigel) substrate, using RNAeasy kit (Qiagen, Valencia, CA, USA) per the manufacturer's instructions. RNA quality control was performed by studying the relative intensity of 18s and 28s rRNA bands using an Agilent 2100 Bioanalyzer and RNA6000 Pico LabChip Kit (Agilent Technologies). Between 200ng and 1ug of RNA were used directly in the TruSeq mRNA stranded kit (Illumina, San Diego, CA) for isolation of mRNA from total RNA, generation of ds cDNA and preparation of libraries. The cDNA was quantified using the Qubit HS DNA kit (Thermo Fisher Scientific, Rockford, IL), and cDNA libraries were prepared using a TruSeq Stranded mRNA library prep kit (Illumina, San Diego, CA). The samples were run on a NextSeq 550 instrument (Illumina, San Diego, CA) with a read length of PE75bp.

RNA-seq analysis

RNA-Seq analysis for 12 conditions (knockouts of KRIT1, CCM2, PDCD10 and non-targeted RNA interference, for cells cultured on 2D surface and in 3D gels for 2 and 6 hours) was performed using raw reads from Illumina NextSeq 550 machine (paired-end reads, 75 bp). BBDuk, BBTools package Version 35.92 [BBMap - Bushnell B. - sourceforge.net/projects/bbmap/] was used for quality control and adapter trimming; TopHat2 v2.1.1 (Kim et al., 2013) was used for transcriptome alignment (Srinivasan et al., 2017). RNA-Seq reads were mapped against the human genome build GRCh38 (Cunningham et al., 2015). We applied GFOLD algorithm (Feng et al., 2012) for biologically meaningful rankings of differentially expressed genes, samples with knockouts were compared with non-targeted RNA interference, and a value of 0.3 was used as a cutoff for generalized fold change. Visualization of gene expression was performed with custom R script. For quantification of pathways enrichment we used David Web Services v6.8 (https://david.ncifcrf.gov/).

Atomic Force Microscopy

Adherent cells were grown on glass FluoroDishes (World Precision Instruments, Sarasota, FL) at 37°C before stiffness measurements were taken. For better global stiffness measurements of the cell, 5.46 µm spherical polystyrene particles were attached to tipless silica nitride cantilevers (MLCT-O10 Bruker Probes, Camarillo, CA) using a two-part epoxy and dried for at least 24 hours. To characterize the mechanical properties of each cell, we used force spectroscopy to obtain force-indentation curves with an atomic force microscope (Asylum Research, Santa Barbara, CA) with an integrated optical microscope (Nikon, Melville, NY) on a vibration isolation table.

Before each day of measurements, the AFM was calibrated by taking a single force curve on a clean FluoroDish to determine the deflection inverse optical lever sensitivity for the particular cantilever. The force exerted on the cell is calculated using Hooke's law which states that $F = k \cdot \Delta x$, using the spring constant found during calibration and the cantilever deflection. For measurements, the cantilever probe was visually aligned with the cell center and moved with a velocity of 2 µm/s to indent the cell with increasing compressive force until a force trigger of 10 nN was reached, completing the approach portion of the force curve, at which point the probe would reverse the direction of its velocity to create the retraction portion of the force curve.

The Hertzian contact model was used to calculate the cellular Young's modulus. The model was fit to the approach or compression segment of the force-indentation curve between 10-90% of the curve where Young's

modulus was independent of indentation. The cells were assumed to be incompressible so that the Poisson's ratio was input into the model as 0.5. We took one measurement per cell and probed 30-50 cells per cell type.

Quantitative Image Analysis of F-actin distribution

For the analysis of the "percent of active area" we quantified the presence of non-contractile actin network at the cell edge. To do this, we subtracted MLC channel from the F-actin channel (both thresholded to eliminate the background fluorescence) for each images cell. Part of the image with co-localized F-actin bindles and MLC cancels out, while the remaining non-zero signal indicates the non-bundled F-actin. In Figure 3 we report the ratio of the area (sum of non-zero pixels) occupied by this non-bundled F-actin within a peripheral strip of 50 pixels (4.3μm) to the total area (sum of both zero and non-zero pixel) of the strip.
For the analysis of the internal distribution of F-actin bundles, we perform the standard texture quantification using the "Contrast" and "Homogeneity" measures. To this end, we constructed the gray-level co-occurrence matrix $p(i,j)$ from each cell image using 8 gray-levels, symmetric ordering, and four offsets in 0, 45, 90, and 135-degree directions. The contrast and homogeneity are defined as $\sum_{i,j}|i-j|^2 p(i,j)$ and $\sum_{i,j}\frac{p(i,j)}{1+|i+j|}$, respectively. In Figure 3, we report the results for the offset distance of 20 pixels (1.72 μm) averaged over the four offset directions. However, the conclusion regarding the significance of the differences in contrast and homogeneity are not sensitive to a choice of the number of gray-levels or the size of the offset.

Quantitative Image Analysis of multicellular formations

A binary mask of the cell formation was formed with a uniform intensity threshold on each field, followed by a manual correction to add back any low-intensity connections that were removed by thresholding but still clearly visible by eye. Small holes in the cellular network from noise or over-thresholding in dimmer areas were filled by a flood-fill operation. Isolated cell objects in the background from the cellular debris were also removed with an area filter. Two features, void area and hole count, were derived from each binary mask through a custom MATLAB script. Void area is the number of pixels belonging to the background in each mask. Holes were defined as continuous regions in the background not divided by cells, tubules, or the image border. The Mean loop count represents the number of these isolated regions in each image. The mean and standard error of these measures were computed for each condition.

Statistical Analysis

Results are expressed as mean ± 2 standard errors unless stated otherwise. Comparisons between groups were analyzed by t-tests. P values <0.05 were considered as statistically significant.

Supplemental References

CUNNINGHAM, F., AMODE, M. R., BARRELL, D., BEAL, K., BILLIS, K., BRENT, S., CARVALHO-SILVA, D., CLAPHAM, P., COATES, G., FITZGERALD, S., GIL, L., GIRON, C. G., GORDON, L., HOURLIER, T., HUNT, S. E., JANACEK, S. H., JOHNSON, N., JUETTEMANN, T., KAHARI, A. K., KEENAN, S., MARTIN, F. J., MAUREL, T., MCLAREN, W., MURPHY, D. N., NAG, R., OVERDUIN, B., PARKER, A., PATRICIO, M., PERRY, E., PIGNATELLI, M., RIAT, H. S., SHEPPARD, D., TAYLOR, K., THORMANN, A., VULLO, A., WILDER, S. P., ZADISSA, A., AKEN, B. L., BIRNEY, E., HARROW, J., KINSELLA, R., MUFFATO, M., RUFFIER, M., SEARLE, S. M., SPUDICH, G., TREVANION, S. J., YATES, A., ZERBINO, D. R. & FLICEK, P. (2015). Ensembl 2015. *Nucleic Acids Res,* 43**,** D662-9.

FENG, J., MEYER, C. A., WANG, Q., LIU, J. S., SHIRLEY LIU, X. & ZHANG, Y. (2012). GFOLD: a generalized fold change for ranking differentially expressed genes from RNA-seq data. *Bioinformatics,* 28**,** 2782-8.

KIM, D., PERTEA, G., TRAPNELL, C., PIMENTEL, H., KELLEY, R. & SALZBERG, S. L. (2013). TopHat2: accurate alignment of transcriptomes in the presence of insertions, deletions and gene fusions. *Genome Biol,* 14**,** R36.

SRINIVASAN, S., SU, M., RAVISHANKAR, S., MOORE, J., HEAD, P., DIXON, J. B. & VANNBERG, F. (2017). TLR-exosomes exhibit distinct kinetics and effector function. *Sci Rep,* 7**,** 41623.